Alternative Organic Spacers for More Efficient Perovskite Solar Cells Containing Ruddlesden-Popper Phases

Xi, Jun; Spanopoulos, Ioannis; Bang, Kijoon; Xu, Jie; Dong, Hua; Yang, Yingguo; Malliakas, Christos D.; Hoffman, Justin M.; Kanatzidis, Mercouri G.; Wu, Zhaoxin

Published in:
Journal of the American Chemical Society

DOI:
10.1021/jacs.0c09647

Publication date:
2020

JACS
JOURNAL OF THE AMERICAN CHEMICAL SOCIETY
pubs.acs.org/JACS
Article

Alternative Organic Spacers for More Efficient Perovskite Solar Cells Containing Ruddlesden–Popper Phases

Jun Xi,[¶] Ioannis Spanopoulos,[¶] Kijoon Bang, Jie Xu, Hua Dong, Yingguo Yang, Christos D. Malliakas, Justin M. Hoffman, Mercouri G. Kanatzidis,[*] and Zhaoxin Wu[*]

Cite This: J. Am. Chem. Soc. 2020, 142, 19705–19714
Read Online
ACCESS | Metrics & More | Article Recommendations | Supporting Information

ABSTRACT: The halide perovskite Ruddlesden–Popper (RP) phases are a homologous layered subclass of solution-processable semiconductors that have aroused great attention, especially for developing long-term solar photovoltaics. They are defined as $(A')_2(A)_{n-1}Pb_nX_{3n+1}$ (A' = spacer cation, A = cage cation, and X = halide anion). The orientation control of low-temperature self-assembled thin films is a fundamental issue associated with the ability to control the charge carrier transport perpendicular to the substrate. Here we report new chemical derivatives designed from a molecular perspective using a novel spacer cation 3-phenyl-2-propenammonium (PPA) with conjugated backbone as a low-temperature strategy to assemble more efficient solar cells. First, we solved and refined the crystal structures of single crystals with the general formula $(PPA)_2(FA_{0.5}MA_{0.5})_{n-1}Pb_nI_{3n+1}$ (n = 2 and 3, space group $C2$) using X-ray diffraction and then used the mixed halide $(PPA)_2(Cs_{0.05}(FA_{0.88}MA_{0.12})_{0.95})_{n-1}Pb_n(I_{0.88}Br_{0.12})_{3n+1}$ analogues to achieve more efficient devices. While forming the RP phases, multiple hydrogen bonds between PPA and inorganic octahedra reinforce the layered structure. For films we observe that as the targeted layer thickness index increases from n = 2 to n = 4, a less horizontal preferred orientation of the inorganic layers is progressively realized along with an increased presence of high-n or 3D phases, with an improved flow of free charge carriers and vertical to substrate conductivity. Accordingly, we achieve an efficiency of 14.76% for planar p–i–n solar cells using PPA-RP perovskites, which retain 93.8 ± 0.25% efficiency with encapsulation after 600 h at 85 °C and 85% humidity (ISOS-D-3).

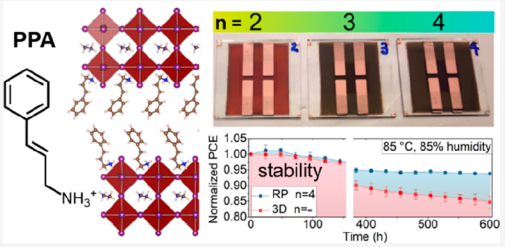

INTRODUCTION

In spite of the recent spectacular progress and development, photovoltaic devices using three-dimensional (3D) organic–inorganic hybrid perovskites (formula AMX_3, A = methylammonium (MA), formamidinium (FA); M = Sn^{2+}, Pb^{2+}; X = Cl^-, Br^-, I^-) still suffer from instability, significantly hindering their access to commercialization.[1−3] It has been shown that oxygen, water, heat, charge, and even synergy effects can dismantle their soft structures.[4−7] Particularly, the $[PbI_6]^{4-}$ unit of the perovskites can easily react with water molecules to form monohydrates and dihydrates, leading to rapid decomposition.[3,8] Many different techniques have been employed to address this critical issue, including adjustment of structural composition, dimensional reduction, and encapsulation of the corresponding devices.[9−16]

Exploiting the hybrid nature of these materials, the introduction of bulky organic countercations into the structure can reduce the dimensionality, giving rise to two-dimensional (2D) layered perovskites. These cations (known as spacers) lay between the inorganic layers, significantly enhancing the moisture resistance, when a hydrophobic linker is used.[17−21] Commonly seen are the Ruddlesden–Popper (RP) phases with the formula $(A')_2(A)_{n-1}Pb_nX_{3n+1}$ (A = MA, FA, cesium (Cs), and their mixtures, X = halide anions), in which monovalent cations (A') generally are bulky ammonium cations.[22−25] In principle, organic spacers with smaller dielectric constants can induce high exciton binding energies and large bandgaps, making a quantum-well-like electronic structure.[26,27] In addition, strong electron–phonon coupling results in pronounced self-trapped excitons, broadening the photoluminescence spectra.[28−32] Moreover, multicolorful light-emitting diodes (LEDs) using RP perovskites have been developed.[33−35] However, strong excitons inhibit the dissociation of charges causing inability to achieve long diffusion lengths within and between layers in the perovskite structure and thus can present an obstacle to efficient solar cells.

The most important property of the two-dimensional perovskites enabling them to form efficient solar cells is the ability to acquire a vertical orientation of the inorganic layers upon film deposition from solutions. This is the key to enable facile charge transport perpendicular to the substrate and across a well-functioning device. Thus, "perpendicular" direction growth of the inorganic $[Pb_nI_{3n+1}]^{(1+n)-}$ slabs is

Received: September 8, 2020
Published: November 4, 2020

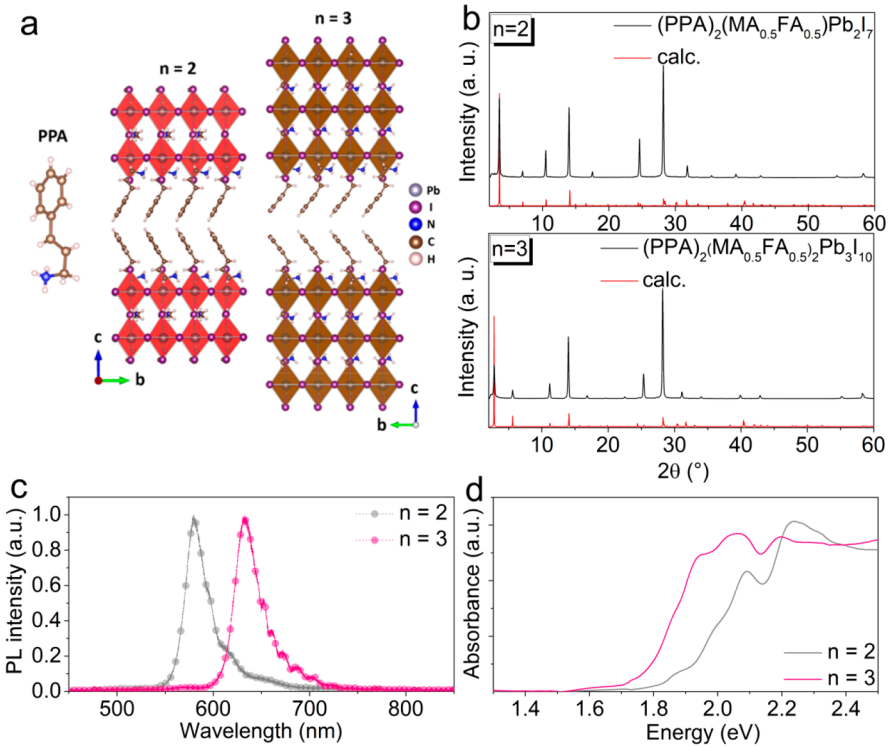

Figure 1. (a) Part of the single crystal structures of the $(PPA)_2(FA_{0.5}MA_{0.5})_{n-1}Pb_nI_{3n+1}$ (n = 2 and 3) materials, looking down the a-axis. (b) Comparison of the PXRD patterns for the as-made single crystals to the calculated patterns based from the solved single crystal structures. (c) Steady-state PL spectra and (d) UV−vis absorption spectra of corresponding single crystals.

preferred for high performance solar cells.[23,36] Until now, the hot-casting method has been the most popular to fabricate perpendicularly orientated inorganic layers.[20] This method, however, limits the development of certain low-temperature processed devices, especially flexible devices. It is worth noting that the most studied RP perovskites used in solar cells involve n-butylammonium (BA) or 2-phenylethylammonium (PEA) organic spacers.[20,37−39] However, versatile organic spacers can be rationally designed to modulate van der Waals and hydrogen-bonding interactions with the inorganic slabs.[40−42] Additionally, certain spacers may be expected to lead to preferred perpendicular orientation of inorganic slabs at low temperatures to achieve high device efficiency.[43−47] Although as a general trend this appears to be the case, it is not known for certain whether the tendency for vertical orientation of the film growth persists regardless of organic spacer or layer thickness. Hence, it is imperative to investigate novel spacers to better understand and control the preferred crystal growth direction.

Here we introduce a custom-made molecule, namely 3-phenyl-2-propenammonium[48] (PPA), serving as an organic conjugated countercation spacer to produce RP perovskites. Single crystal structure analyses reveal strongly stabilized RP structures thanks to multiple types of hydrogen contact between PPA and inorganic octahedra. As for their films, when the thickness n of the inorganic slabs increases from 2 to 4, the low-temperature assembled RP films demonstrate progressively less horizontal preferred crystal growth and increased fractions of high-n (or 3D-like) phases. Meanwhile, with increasing n, the dominant excitons become less strongly bonded to more easily give free carriers, and the vertical film conductivity follows an increasing trend. We grew single crystals of $(PPA)_2(FA_{0.5}MA_{0.5})_{n-1}Pb_nI_{3n+1}$ (n = 2, 3) and solved their crystal structure using X-ray diffraction analysis. We find that using the mixed halide isostructural $(PPA)_2(Cs_{0.05}(FA_{0.88}MA_{0.12})_{0.95})_{n-1}Pb_n(I_{0.88}Br_{0.12})_{3n+1}$ analogues leads to better device fabrication. We show that assembling PPA-RP perovskite ($n \leq 4$) films into low-temperature planar p−i−n structured solar cells produces highly effective and stable multiphase 2D/3D composite that results in a champion power conversion efficiency (PCE) of 14.76% with negligible hysteresis when scanning forward/reverse current density−voltage (J−V) direction. Importantly, after 600 h at 85 °C and 85% humidity (ISOS-D-3), the efficiency of the encapsulated PPA-RP perovskite solar cell (n = 4) retained 93.8 ± 0.25% of its original value compared to 84.7 ± 1.9% for a pure 3D counterpart stored under the same conditions. This work highlights the significance of selecting proper organic spacers to control the crystal growth direction and charge transport of RP perovskite films and addresses a critical concern of applying 2D layered perovskites in photovoltaics.

RESULTS AND DISCUSSION

Synthesis and Characterization of PPA-RP Perovskites. Initially, we wanted to verify whether the PPA organic spacer cation can give rise to uniform high quality stable 2D RP perovskites. Off-stoichiometric reactions in acidic media[25] gave rise to high quality pure iodide single crystals with the general formula $(PPA)_2(FA_{0.5}MA_{0.5})_{n-1}Pb_nI_{3n+1}$ (n = 2 and 3). Single crystal X-ray diffraction (XRD) studies (see the Supporting Information) verify that the corresponding materials indeed belong to the RP family of perovskites, since the structure consists of 2D inorganic layers of corner-sharing $[PbI_6]^{4-}$ octahedra which are separated by two layers of organic phenylpropylene ammonium cations (PPA^+), and

https://dx.doi.org/10.1021/jacs.0c09647
J. Am. Chem. Soc. 2020, 142, 19705−19714

adjacent inorganic layers are shifted by 1/2 unit cell length (Figure 1a and Figure S1).[49] Dispersion interactions (between the carbon chains) and electrostatic interactions (between the ammonium heads and anionic perovskite layers) stabilize the structure. The small FA and MA cations reside in the cavities formed by the inorganic octahedra, charge balancing the framework, in a similar manner as in the case of the 3D perovskites. Crystallographic details and structure refinement for all the single crystals are summarized in Table 1. Both

Table 1. Crystallographic Details and Structure Refinement for the Single Crystals of $(PPA)_2(FA_{0.5}MA_{0.5})_{n-1}Pb_nI_{3n+1}$ RP Perovskites[a]

	compound (293 K)	
	$(PPA)_2(MA_{0.5}FA_{0.5})Pb_2I_7$	$(PPA)_2(MA_{0.5}FA_{0.5})_2Pb_3I_{10}$
empirical formula	$C_{19}H_{31}I_7N_3Pb_2I_7$	$C_{20}H_{40}I_{10}N_4Pb_3I_{10}$
formula weight	1604.2	2227.2
crystal system	monoclinic	monoclinic
space group	*C*2	*C*2
color	red	dark brown
unit cell dimensions	a = 8.9424 Å	a = 8.9297 Å
	b = 8.9425 Å	b = 8.928 Å
	c = 25.5898 Å	c = 31.8692 Å
	α = 90°	α = 90°
	β = 100.048°	β = 98.0193°
	α = 90°	γ = 90°
volume (Å^3)	2014.963	2515.906
Z	2	2
density (calcd, g/cm^3)	2.644	2.94
absorption coefficient (mm^{-1})	13.718	16.164
F(000)	1354	1908
θ range for data collection	1.616°−29.366°	3.228°−30.728°
index ranges	$-11 \le h \le 12$	$-12 \le h \le 12$
	$-10 \le k \le 12$	$-10 \le k \le 12$
	$-35 \le l \le 34$	$-45 \le l \le 44$
reflections collected	8826	8361
independent reflections	4820 [R_{int} = 0.1195]	5944 [R_{int} = 0.0433]
completeness to θ = 25.242°	99.6%	99.3%
data/restraints/parameters	4820/34/77	5944/146/150
goodness of fit	0.933	1.040
final R indices [$I > 2\sigma(I)$]	R_{obs} = 0.0789	R_{obs} = 0.0747
	wR_{obs} = 0.2008	wR_{obs} = 0.1926
R indices [all data]	R_{all} = 0.2494	R_{all} = 0.1103
	wR_{all} = 0.2776	wR_{all} = 0.2143
largest diff peak and hole (e Å^{-3})	1.301 and −0.989	3.366 and −3.131

[a] $R = \sum||F_o| - |F_c||/\sum|F_o|$, $wR = \{\sum[w(|F_o|^2 - |F_c|^2)^2]/\sum[w(|F_o|^4)]\}^{1/2}$, and $w = 1/(\sigma^2(I) + 0.0004I^2)$.

crystal structures crystallize in the monoclinic *C*2 space group. Powder XRD measurements verified the uniform phase purity of the corresponding bulk samples since the calculated and experimental patterns match exactly (Figure 1b). ^{1}H NMR (nuclear magnetic resonance) analysis was done by dissolving the as-made crystals in DMSO-d_6, providing an evidence of the incorporation of both MA and FA cations in the crystal structure (Figures S2 and S3). Scanning electron microscopy (SEM) measurements (Figure S4) reveal uniform smooth platelike crystals for the PPA-RP family, typical for 2D hybrid halide perovskites.

A most unusual feature of this structure is the fact that the organic spacer protrudes much deeper into the grooves formed by the terminal iodide atoms of the $[PbI_6]^{4-}$ octahedra compared to other RP structures based on similar bulky linkers (e.g., (FPEA = 4-$FC_6H_4(CH_2)_2NH_3^+$).[50] This behavior stems from the presence of the double bond (−CH═CH−) with sp^2 hybridization, which generates extra notable hydrogen contacts with the I^- anions of the inorganic octahedra (see Figure S5). Specifically, there is one hydrogen bond among the hydrogens of the R−NH_3^+ group and the bridging equatorial iodide anions (−NH···I) laying at a distance of 2.658(15) Å, a second longer (−CH_2···I) contact among the methylene hydrogens and the bridging equatorial iodide anions laying at a distance of 3.003(10) Å, and a third (−CH···I) contact among the ethylene hydrogens and the axial iodide anions at 3.121(18) Å. Despite the large number of (−NH···I) hydrogen bonds and (−CH···I) contacts, the inorganic octahedra are not distorted, as in the case of (3AMPY)$(MA)_{n-1}Pb_nI_{3n+1}$2D perovskites (3AMPY = 3-(aminomethyl)pyridinium)),[51] presumably because of the presence of the rigid, bulkier than MA, FA cations in the cuboctahedral cavities. The different manner in which the PPA spacers interact with the inorganic octahedra leads to less distortion, and hence, the Ruddlesden−Popper structure can be stabilized.

The recorded trends in the absorption and photoluminescence (PL) emission spectra (Figure 1c,d) suggest a progressively reduced bandgap as n increases because of less quantum and dielectric confinement.[52,53] Apparently, the presence of the FA cation in the cuboctahedral cavities of the inorganic layers affects greatly the optical properties by suppressing any octahedral distortion compared to MA-only based samples. Notably, taking a closer look at the equatorial and axial Pb−I−Pb angles of $(PPA)_2(MA_{0.5}FA_{0.5})_2Pb_3I_{10}$, they are almost linear with values of 179.9(4)° and 176.4(4)°, respectively. For comparison, $(HA)_2(MA)_2Pb_3I_{10}$ (HA = hexylamine) contains only MA cations and has a much larger octahedral distortion with axial and equatorial Pb−I−Pb angles of 167.28(10)° and 167.52(6)°, respectively.[25] For these reasons the bandgap of $(PPA)_2(MA_{0.5}FA_{0.5})_2Pb_3I_{10}$ is slightly red-shifted in comparison to the bandgap of $(HA)_2(MA)_2Pb_3I_{10}$, with values of 1.94 and 1.98 eV, respectively, based on the excitonic edges.[54]

Film Deposition of PPA-RP Perovskites. Given the nonideal optical properties for photovoltaics and unfavorable crystallization kinetics of pure iodide lattice, we adopted mixed iodide and bromide lattice for the film fabrication. Meanwhile, mixed cations in the perovskite cage can further stabilize the 2D lattice. Hence, different from the pure iodide single crystals, the corresponding assembled PPA-RP thin films are based on a chemical formula of isostructural $(PPA)_2(Cs_{0.05}(FA_{0.88}MA_{0.12})_{0.95})_{n-1}Pb_n(I_{0.88}Br_{0.12})_{3n+1}$ (in the following text abbreviated as $(PPA)_2(Cs/FA/MA)_{n-1}Pb_n(I/Br)_{3n+1}$), where the ratios between Cs/FA/MA and I/Br are fixed to the optimal 0.05/0.836/0.114 and 0.88/0.12, respectively.[55] The detailed compositions of the corresponding precursors can be found in Table S11. The results on FA/MA ratios can be found in Figure S6.

The corresponding RP perovskite films were deposited on substrates by simple spin-coating at room temperature (instead of the hot-casting method). The properties of the n = 1 sample clearly reveal the well-defined single-layered RP structure

https://dx.doi.org/10.1021/jacs.0c09647
J. Am. Chem. Soc. 2020, 142, 19705−19714

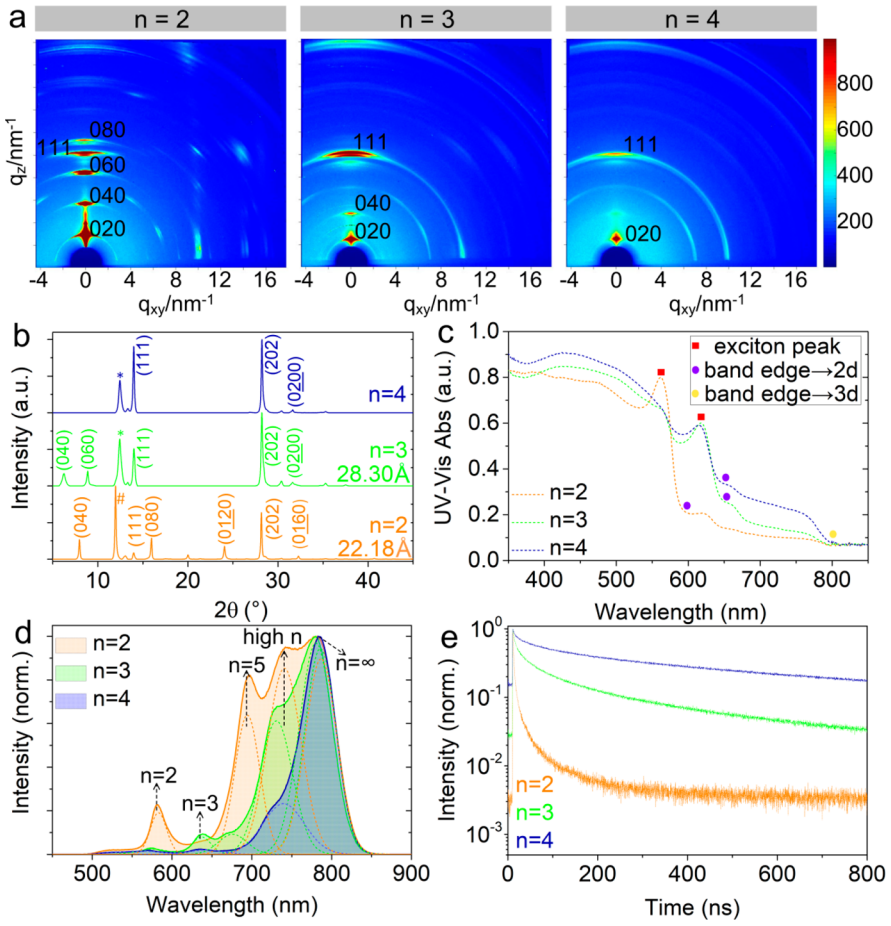

Figure 2. (a) GIWAXS patterns of $(PPA)_2(Cs/FA/MA)_{n-1}Pb_n(I/Br)_{3n+1}$ ($n \leq 4$) films. (b) XRD patterns of $(PPA)_2(Cs/FA/MA)_{n-1}Pb_n(I/Br)_{3n+1}$ ($n \leq 4$) films. In XRD patterns, "∗" and "#" denotes δ-$FAPbI_3$ and excess PbI_2. In addition, the (020) plane distance of $n = 2$ and 3 is shown as 22.18 and 28.30 Å, respectively (fitted by MDI Jade 6.5). For $n = 4$, the (0k0) plane is from $n = 3$ phases. (c) UV−vis absorption spectra, (d) steady-state PL spectra, and (e) time-resolved PL spectra of the corresponding films.

(Figure S7). Figure 2a shows grazing-incidence wide-angle X-ray scattering (GIWAXS) patterns of PPA-RP perovskite films. For $n = 2$, the peaks along the q_z-axis correspond to the basal (0k0) planes. The presence of (0k0) plane Bragg reflections along the q_z-axis suggests the layers are oriented parallel to the substrate. However, the peaks have broadened arcs, indicating less perfectly horizontal oriented layers. Simulating the $n = 2$ film with a parallel orientation (Figure S8) shows that the peaks do not perfectly match the GIWAXS pattern. The peaks are seen at higher q_z values than anticipated, indicating a smaller unit cell than expected. Because the layers are parallel to the substrate, this indicates that the unit cell is compressed along the c-axis through the layers. This is a possible result of the addition of Cs^+, MA^+, and Br^- ions in the films. Additional peaks along the q_z-axis at $q = \sim 4$ and ~ 8 nm^{-1} do not match the pattern for $n = 2$ and may be from another phase such as $n = 1$ or a lower dimensional structure. For $n = 3$, the peaks are accompanied by rings which indicate there are both grains parallel to the substrate and oriented grains. Here, two secondary phases are seen: $n = 2$ and the same unknown phase from the $n = 2$ film. Like the $n = 2$ film, the film for $n = 3$ has a compressed unit cell along the c-axis compared to the simulated pattern in Figure S8. The same is seen for $n = 4$, but the major peaks correspond to $n = 3$ and the rings are very broad. This broadness makes it difficult to distinguish any higher n phases present. Moreover, XRD patterns in Figure 2b, similar to GIWAXS patterns, validate the varied orientation and change in unit cell compared to the XRD of the crystals (Figure 1b). We can draw conclusions from the data as follows: (1) The sharp Bragg peaks in the patterns of the $n = 2$ sample are more well-defined than that of the higher n films, which begin to show Debye−Scherrer rings for $n = 3$ and 4. This variation indicates that as the n value increases, the films evolve into less oriented and less crystalline films.[56,57] (2) As n varies from 2 to 4, the strong orientation of most (0k0) planes gradually diminishes along the q_z direction, indicating suppressed horizontal orientation. This could be also caused by lower phase purity compared to single crystals. In the high n (like $n = 4$) films, because of the observed less ordered pure phases, we deduce greater percentage of high-n (or 3D-like) phases formed. (3) For $n = 2$, 3, and 4, the intensity of (111) diffraction ring reaches a peak at 90° of azimuthian angle (Figure S9). In particular, for $n = 4$, the arc at 90° in (111) rings seems relatively pure without noticeable arcs at other degrees.[58]

The above results imply that the high-n samples have a higher degree of vertical orientation and contain some even higher-n (or even 3D-like) phases. The possible origin is deduced as follows: For the assembled PPA-RP perovskite film, as the layers become thicker ($n > 1$), a competition emerges between the organic spacers confining the in-plane growth and the FA/MA ions expanding the out-of-plane growth.[18] The

https://dx.doi.org/10.1021/jacs.0c09647
J. Am. Chem. Soc. 2020, 142, 19705−19714

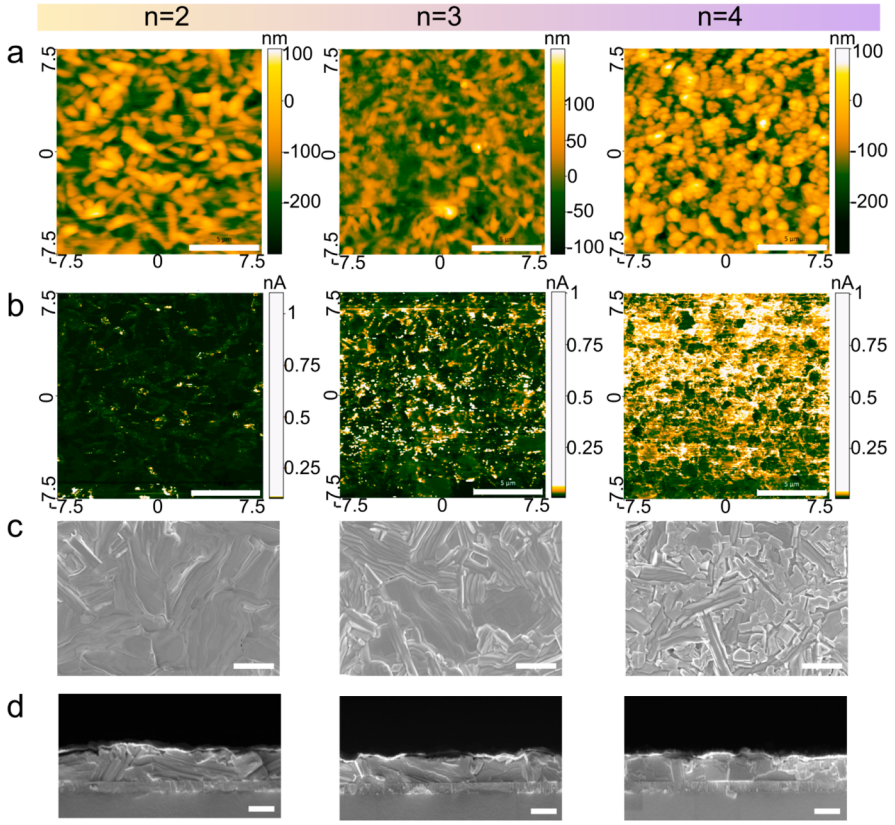

Figure 3. (a) AFM images (scale bar: 5 μm), (b) c-AFM images (current unit: nA; scale bar: 5 μm), (c) top-view (scale bar: 1 μm), and (d) cross-sectional (scale bar: 500 nm) SEM images of $(PPA)_2(Cs/FA/MA)_{n-1}Pb_n(I/Br)_{3n+1}$ ($n \leq 4$) films.

netlike hydrogen bonds formed between PPA and the inorganic slabs (discussed above) can suppress the tendency for in-plane orientation by helping to better connect the neighboring sheets. Hence, in the low-temperature assembled thicker layer PPA-RP perovskites, the relatively long conjugated PPA can inhibit the horizontal crystal growth of higher-n phases with respect to the substrate.

Figure 2c shows the UV−vis absorption spectra of different layered PPA-RP perovskite films.[19,25] The three films exhibit two band edges: one 2D feature located at short wavelength (around 600 nm for n = 2 and 650 nm for n = 3, 4) and another 3D-like band edge emerged at around 795 nm, indicating a local band gap of about 1.56 eV. Meanwhile, as n increases from 2 to 4, the 3D-like band edge becomes more pronounced, implying the dissociation onto 3D and other 2D phases creates a 2D/3D composite film. The presence of 2D phases is shown from the exclusive exciton peaks assigned at 562 nm (2.20 eV) and 615 nm (2.01 eV), which could be explained by the n = 2 and 3 members of the family. For n = 4, an exciton peak near n = 3 is found, suggesting the presence of n = 3 RP structures in the film, which is consistent with the GIWAXS results above. All these results are in agreement with what we observed from GIWAXS above. All the evidence suggests that with increasing n there is an increase in preferred perpendicular orientation and formation of high-n (or 3D-like) phases.

The steady-state PL spectra of the films are shown in Figure 2d. In the n = 2 sample, a complex PL spectrum appears, which seems like an accumulation of multiple exciton radiative recombination from hybrid 2D perovskites with different n values. As n increases, the number of peaks in the spectra is gradually diminishing. On the basis of the PL peak positions, we used multiple peak fittings to understand the respective PL spectra in the thicker layered films (Figure 2b). Although some 2D featured PL peaks are seen from 550 to 750 nm, the 3D featured PL peak strongly dominates, especially when n increases to 4. This trend verifies the hybrid 2D/3D composite nature of the films.

To understand the charge carrier dynamics of different layered PPA-RP perovskite films, we measured the time-resolved PL (TRPL) spectra at the main steady-state PL peak, the results of which are summarized in Figure 2e. The background level should be solely dominated by the collected photon counting, which is reflected by the y-axis. Notably, the y-axis is in log scale, which amplifies the weaker signal especially with several orders of magnitude smaller intensity. In this fashion, the faster decay curves appear to have the noiselike background level. Figure S11 shows the exponentially fitted results of these spectra. For the n = 2 film, much shorter average carrier lifetimes (τ_{ave}) are found. However, τ_{ave} significantly increases as n increases to 3 and 4. Here we realize that the monomolecular recombination rate (k_1, derived from fitted results) of n = 2 is 0.96×10^9 s^{-1}, 1 order of magnitude higher than that of n = 3 and 4 (2.4×10^8 and 1.7×10^8 s^{-1}, respectively). This difference can be accounted for by the much higher exciton binding energy (>200 meV) in existing thinner (n = 2) layered slabs, which allows for an additional monomolecular recombination pathway.[59] Therefore, the thicker layered ($n \geq 3$) PPA-RP perovskite films are the most promising for efficient solar cells.

We then measured the topography and conductivity of the series of PPAI-RP perovskite films. Figures 3a and 3b show the

https://dx.doi.org/10.1021/jacs.0c09647
J. Am. Chem. Soc. 2020, 142, 19705−19714

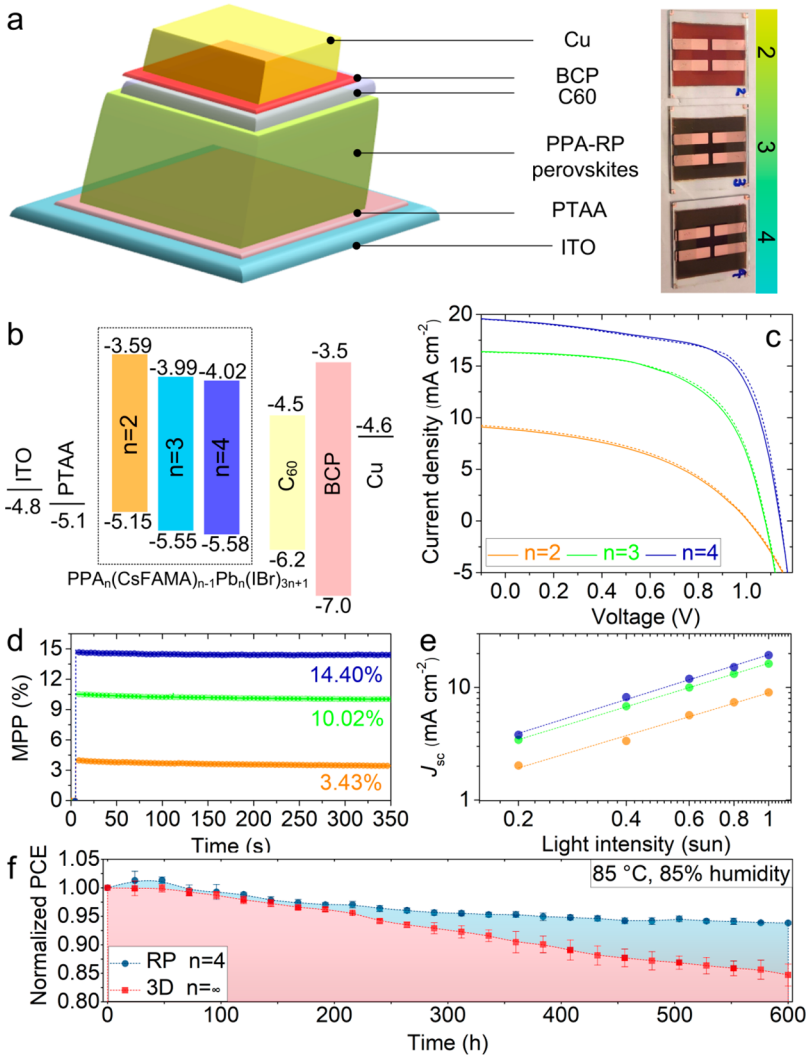

Figure 4. (a) Device structure and digital photos of assembled p−i−n solar cells based on $(PPA)_2(Cs/FA/MA)_{n-1}Pb_n(I/Br)_{3n+1}$ ($n \leq 4$) films. (b) Energy alignment of the fabricated devices. The energy levels are extracted from UPS data of the films (see Figure S12). (c) $J-V$ curves of the best PPA-RP ($n \leq 4$) solar cells. (d) Maximum power point (MPP) tracking following the voltage at PCE. (e) Light intensity dependent short-circuit current density (J_{sc}) of the best PPA-RP ($n \leq 4$) solar cells. (f) Stability of encapsulated devices based on PPAI-RP ($n = 4$) and 3D ((Cs/FA/MA)Pb(I/Br)) perovskites tested at 85 °C and 85% humidity.

atomic force microscopy (AFM) and conductivity-AFM (c-AFM) micrographs, respectively. For $n = 2$, the crystallites form as discrete small stripelike domains along with a fraction of smaller grains. This topography indicates that a minority of $[(Cs/FA/MA)_{n-1}Pb_n(I/Br)_{3n+1}]^{2-}$ units is emerging in a relatively perpendicular direction. Interestingly, the perpendicular crystal orientation results in average current (I_{ave}) of 50 pA, but the current distribution is nonuniform, mainly located at the smaller domains. For $n = 3$, smaller crystal domains form along some which exhibit the stripe textures. More importantly, the I_{ave} significantly increases to 181 pA with higher uniformity, in good agreement with reduced horizontal orientation of inorganic slabs. Particularly, when n reaches 4, highly homogeneous and dense domains occupy the whole film with negligible stripelike textures, corresponding to the highest I_{ave} of 216 pA with uniform c-AFM map. The highest current and uniform distribution of $n = 4$ originates from highly reduced horizontal orientation and considerable high-n (or 3D-like) phases. The high- and low-magnification scanning electron microscopy (SEM) images of Figure 3c and Figure S12 confirm the gradual disappearance of stripe textured needle crystals with a ratio of 55.15%, 28.66%, and 4.43% and an emergence of smaller sized domains as n increases. The high-n films also exhibit greatly reduced roughness (Figure S13). Furthermore, the film thickness is estimated to around 580 nm ($n = 2$), 470 nm ($n = 3$), and 440 nm ($n = 4$) from the cross-sectional SEM images (Figure 3d). The data presented above, in regards to both the crystal topography and conductivity, corroborate the progressively rotating direction of quantum wells and being formed 2D/3D hybrids, which is further backed up by the GIWAXS results.

Device Fabrication of PPA-RP Perovskites. Solar cells were fabricated to test the effect of the orientation on device efficiency. In terms of device structure, a low-temperature processed planar p−i−n architecture is adopted, consisting of ITO (indium tin oxide) (160 nm)/PTAA (poly(bis(4-phenyl)(2,4,6-trimethylphenyl)amine)) (8 nm)/PPA-RP perovskites/C_{60}(20 nm)/BCP (bathocuproine) (6 nm)/Cu (80 nm). The procedure of device fabrication is summarized in the Experimental Section. Here, the 2D PPA-RP perovskites give

https://dx.doi.org/10.1021/jacs.0c09647
J. Am. Chem. Soc. 2020, 142, 19705−19714

the average formula of $(PPA)_2(Cs_{0.05}(FA_{0.88}MA_{0.12})_{0.95})_{n-1}Pb_n(I_{0.88}Br_{0.12})_{3n+1}$, matching that in the film deposition part. Notably, the hot-casting method and traditional organic spacers are inferior to the low-temperature PPA strategy (Figure S14). Figures 4a and 4b demonstrate the fabricated device structure and its energy alignment, whose band levels are acquired from the UPS spectra of the films (Figure S15). In addition, the digital photos of corresponding devices are listed in Figure 4a, where highly homogeneous perovskite films can be observed. The estimated valence bands should be from the 3D-like phase, which is consistent with the PL and optical absorption data presented above.[60] The statistics of all the photovoltaics parameters are summarized in Table 2 and Figure S16. When n = 2, the open-circuit voltage (V_{oc}) has a decent value of 1.02 ± 0.03 V. This is caused by less strongly bonded excitons from the increased quantum well thickness and prolonged carrier lifetime from the decreased horizontal orientation. Nevertheless, because the majority of the layers are parallel to the substrate, the short-circuit current density (J_{sc}) and fill factor (FF) are relatively low. For n = 3, the J_{sc} and FF are significantly improved as a result of suppressed non-radiative recombination as well as increased out-of-plane conductivity. The maximum performance of these solar cells is obtained for n = 4, benefiting from the long-lived carriers and superior conductivity in this member and higher-n 3D-like members present, which is also aided by the more vertical orientation of the layers relative to the substrate.

Table 2. Statistics of Photovoltaic Parameters of the Low-Temperature p−i−n Solar Cells Based on Different PPA-RP Perovskites

n	J_{sc} (mA cm^{-2})	V_{oc} (V)	FF (%)	PCE (%)
2	8.14 ± 0.51	1.02 ± 0.03	40.39 ± 2.16	3.35 ± 0.32
3	15.71 ± 0.30	1.07 ± 0.02	56.79 ± 1.35	9.60 ± 0.44
4	18.72 ± 0.44	1.14 ± 0.01	66.19 ± 0.90	14.16 ± 0.32

The J−V curves of the champion solar cells based on all three PPA-RP perovskites are given in Figure 4c. The detailed parameters of corresponding devices are also concluded in Table 3. One can easily observe negligible hysteresis between the forward and reverse sweeps. In addition, the external quantum efficiency (EQE) spectra (Figure S17) confirm the reliability of J_{sc} from J−V curves. Importantly, we have achieved a champion PCE of 14.76%, with a J_{sc} of 19.33 mA/cm^2, V_{oc} of 1.14 V, and FF of 0.67, respectively, for the n = 4 device. To our knowledge, this distinguished performance is one of the highest efficiencies reported for low-temperature processed solar cells using self-assembled RP (nominal $n \leq 4$) perovskites (Table S12).

Table 3. Photovoltaic Parameters of the Best Low-Temperature p−i−n Solar Cells Based on Different PPA-RP Perovskites

n	scanning direction	J_{sc} (mA cm^{-2})	V_{oc} (V)	FF (%)	PCE (%)
2	forward	8.89	1.00	43.2	3.84
	reverse	9.05	1.00	43.7	3.96
3	forward	16.33	1.08	58.0	10.23
	reverse	16.29	1.08	59.4	10.46
4	forward	19.40	1.14	65.3	14.45
	reverse	19.33	1.14	67.0	14.76

Moreover, the maximum power point tracking (MPP) tests of these champion devices in Figure 4d and Figure S18 show highly stable power output, verifying these high photovoltaic performances. To understand the charge recombination in the PPA-RP perovskite based working devices, light-intensity-dependent J−V measurements have been carried out, as shown in Figure S19. Figure 4e shows the extracted J_{sc} vs I_{int} (light intensity) using double-logarithmic scales. Theoretically, when the slope α (J_{sc}/I_{int} by linear fitting) approaches 1, the device works more like an ideal diode without charge recombination. Here the α value of the device based on n = 2, 3, and 4 is 0.95, 0.97, and 0.99, respectively, revealing an increasingly efficient charge collection. This trend is in good agreement with the variation of the device performance. As is known, RP perovskites can greatly endure high humidity.[20] Here, the mixed triple cations within the layers are also expected to enhance the device thermal stability.[9] To validate the humidity and thermal stability, the encapsulated solar cells based on PPA-RP (n = 4) perovskite and 3D perovskite are stored in a chamber of 85 °C and 85% humidity (ISOS-D-3) to track the device performance. Figure 4f summarizes the statistical normalized PCE over time. The photovoltaic parameters of the best devices before and after the aging tests are also given in Table S13. After 600 h, PPA-RP perovskite-based device could maintain 93.8 ± 0.25% of the starting efficiency. However, the 3D perovskite based device retained only 84.7 ± 1.9%. Moreover, the nonencapsulated PPA-RP perovskite-based device showed higher aqueous stability than the 3D one (Figure S20). These distinctions highlight the promise for excellent environmental stability of 2D PPA-RP perovskites and use in practical applications.

CONCLUSIONS

We have used a novel custom-made organic conjugated molecule, 3-phenyl-2-propenammonium (PPA), as a spacer for the synthesis of new series of layered Ruddlesden−Popper (RP) perovskites, specifically single crystals with the formula $(PPA)_2(FA_{0.5}MA_{0.5})_{n-1}Pb_nI_{3n+1}$ (n = 2, 3). The solved crystal structures reveal multiple hydrogen bonds and contacts between the PPA spacers and inorganic units. We also prepared analogous mixed iodide/bromide thin film assemblies formulated as $(PPA)_2(Cs_{0.05}(FA_{0.88}MA_{0.12})_{0.95})_{n-1}Pb_n(I_{0.88}Br_{0.12})_{3n+1}$ (n = 2−4) which are preferable for better performing devices. The use of PPA for the generation of fully 2D based perovskite devices with optimum layer orientation is possible, paving the way for the use of more elaborate organic linkers with tunable functionalities. The corresponding thin films were utilized for a systematic study of composition and orientation of the layers with varying n. The PPA ligand can indeed direct the preferred crystal growth of the inorganic perovskite layers diminishing the horizontal orientation and producing films with considerable high-n (or 3D-like) domains for n > 2. Utilization of the layered PPA-RP perovskite film for n = 4 composition gave rise to a champion efficiency of 14.76% for p−i−n solar cells. Impressively, the very high efficiency of the encapsulated PPA-RP perovskite solar cell was tested for 600 h at 85 °C and 85% humidity (ISOS-D-3) and maintained 93.8 ± 0.25% of its initial value as compared to 84.7 ± 1.9% for the 3D analogue.

https://dx.doi.org/10.1021/jacs.0c09647
J. Am. Chem. Soc. 2020, 142, 19705−19714

■ ASSOCIATED CONTENT

Supporting Information

The Supporting Information is available free of charge at https://pubs.acs.org/doi/10.1021/jacs.0c09647.

Materials and methods, synthetic details, additional supplementary figures and tables about material characterization, ^{1}H NMR measurements, SEM/EDS measurements, XPS measurements, GIWAXS measurements, TRPL measurements, AFM measurements, UPS measurements, tested device data, EQE spectra, current density output, light-intensity dependent $J-V$ curves and aqueous stability of the nonencapsulated devices (PDF)

X-ray crystallographic data for $(PPA)_2(MA_{0.5}FA_{0.5})Pb_2I_7$ (CIF)

X-ray crystallographic data for $(PPA)_2(MA_{0.5}FA_{0.5})_2Pb_3I_{10}$ (CIF)

■ AUTHOR INFORMATION

Corresponding Authors

Mercouri G. Kanatzidis − *Department of Chemistry, Northwestern University, Evanston, Illinois 60208, United States;* orcid.org/0000-0003-2037-4168; Email: m-kanatzidis@northwestern.edu

Zhaoxin Wu − *Key Laboratory for Physical Electronics and Devices of the Ministry of Education & Shaanxi Key Lab of Information Photonic Technique, School of Electronic and Information Engineering, Xi'an Jiaotong University, Xi'an 710049, P. R. China; Collaborative Innovation Center of Extreme Optics, Shanxi University, Taiyuan 030006, P. R. China;* Email: zhaoxinwu@mail.xjtu.edu.cn

Authors

Jun Xi − *Global Frontier Center for Multiscale Energy Systems, Seoul National University, Seoul 08826, South Korea; Zernike Institute for Advanced Materials, University of Groningen, 9747 AG Groningen, The Netherlands;* orcid.org/0000-0001-6600-4862

Ioannis Spanopoulos − *Department of Chemistry, Northwestern University, Evanston, Illinois 60208, United States;* orcid.org/0000-0003-0861-1407

Kijoon Bang − *Global Frontier Center for Multiscale Energy Systems, Seoul National University, Seoul 08826, South Korea;* orcid.org/0000-0001-6877-9792

Jie Xu − *Key Laboratory for Physical Electronics and Devices of the Ministry of Education & Shaanxi Key Lab of Information Photonic Technique, School of Electronic and Information Engineering, Xi'an Jiaotong University, Xi'an 710049, P. R. China;* orcid.org/0000-0002-9857-2212

Hua Dong − *Key Laboratory for Physical Electronics and Devices of the Ministry of Education & Shaanxi Key Lab of Information Photonic Technique, School of Electronic and Information Engineering, Xi'an Jiaotong University, Xi'an 710049, P. R. China; Collaborative Innovation Center of Extreme Optics, Shanxi University, Taiyuan 030006, P. R. China;* orcid.org/0000-0001-9362-2236

Yingguo Yang − *Shanghai Synchrotron Radiation Facility, Shanghai Institute of Applied Physics, Chinese Academy of Sciences, Shanghai 201204, P. R. China;* orcid.org/0000-0002-1749-2799

Christos D. Malliakas − *Department of Chemistry, Northwestern University, Evanston, Illinois 60208, United States;* orcid.org/0000-0003-4416-638X

Justin M. Hoffman − *Department of Chemistry, Northwestern University, Evanston, Illinois 60208, United States;* orcid.org/0000-0003-1400-9180

Complete contact information is available at: https://pubs.acs.org/10.1021/jacs.0c09647

Author Contributions

¶J.X. and I.S. contributed equally to this work.

Notes

The authors declare no competing financial interest.

■ ACKNOWLEDGMENTS

This work was supported in part by the National Natural Science Foundation of China (Grants 11574248 and 61505161). China Postdoctoral Science Foundation (Grant 2016M590947), Scientific Research Plan Projects of Shaanxi Education Department (Grant 17JK0700), Natural Science Basic Research Plan in Shaanxi Province of China (Grant 2019JQ-119), and Fundamental Research Funds for the Central Universities (Grant xjj2016031). J.X. and K.B. acknowledge support from the Global Frontier R&D Program of the Center for Multiscale Energy System (Grant 2012M3A6A7054855) by the National Research Foundation under the Ministry of Education, Science and Technology, Korea. The work on perovskite solar cells at Northwestern University was supported by ONR Grant N00014-20-1-2725. This work made use of the IMSERC and EPIC facilities at Northwestern University, which have received support from the SHyNE Resource (NSF ECCS-1542205), the IIN, and Northwestern's MRSEC program (NSF DMR-1720139), the State of Illinois, and Northwestern University.

■ REFERENCES

(1) Correa-Baena, J.-P.; Saliba, M.; Buonassisi, T.; Grätzel, M.; Abate, A.; Tress, W.; Hagfeldt, A. Promises and challenges of perovskite solar cells. *Science* **2017**, *358*, 739−744.

(2) Boyd, C. C.; Cheacharoen, R.; Leijtens, T.; McGehee, M. D. Understanding degradation mechanisms and improving stability of perovskite photovoltaics. *Chem. Rev.* **2019**, *119*, 3418−3451.

(3) Manser, J. S.; Saidaminov, M. I.; Christians, J. A.; Bakr, O. M.; Kamat, P. V. Making and breaking of lead halide perovskites. *Acc. Chem. Res.* **2016**, *49*, 330−338.

(4) Yang, J.; Siempelkamp, B. D.; Liu, D.; Kelly, T. L. Investigation of $CH_3NH_3PbI_3$ degradation rates and mechanisms in controlled humidity environments using in situ techniques. *ACS Nano* **2015**, *9*, 1955−1963.

(5) Aristidou, N.; Sanchez-Molina, I.; Chotchuangchutchaval, T.; Brown, M.; Martinez, L.; Rath, T.; Haque, S. A. The role of oxygen in the degradation of methylammonium lead trihalide perovskite photoactive layers. *Angew. Chem., Int. Ed.* **2015**, *54*, 8208−8212.

(6) Divitini, G.; Cacovich, S.; Matteocci, F.; Cinà, L.; Di Carlo, A.; Ducati, C. In situ observation of heat-induced degradation of perovskite solar cells. *Nat. Energy* **2016**, *1*, 15012.

(7) Ahn, N.; Kwak, K.; Jang, M. S.; Yoon, H.; Lee, B. Y.; Lee, J.-K.; Pikhitsa, P. V.; Byun, J.; Choi, M. Trapped charge-driven degradation of perovskite solar cells. *Nat. Commun.* **2016**, *7*, 13422.

(8) Huang, J.; Tan, S.; Lund, P. D.; Zhou, H. Impact of H_2O on organic-inorganic hybrid perovskite solar cells. *Energy Environ. Sci.* **2017**, *10*, 2284−2311.

(9) Saliba, M.; Matsui, T.; Seo, J.-Y.; Domanski, K.; Correa-Baena, J.-P.; Nazeeruddin, M. K.; Zakeeruddin, S. M.; Tress, W.; Abate, A.; Hagfeldt, A.; Grätzel, M. Cesium-containing triple cation perovskite solar cells: improved stability, reproducibility and high efficiency. *Energy Environ. Sci.* **2016**, *9*, 1989−1997.

(10) Dong, H.; Xi, J.; Zuo, L.; Li, J.; Yang, Y.; Wang, D.; Yu, Y.; Ma, L.; Ran, C.; Gao, W.; Jiao, B.; Xu, J.; Lei, T.; Wei, F.; Yuan, F.; Zhang, L.; Shi, Y.; Hou, X.; Wu, Z. Conjugated molecules "bridge": functional ligand toward highly efficient and long-term stable perovskite solar cell. *Adv. Funct. Mater.* **2019**, *29*, 1808119.
(11) Bai, S.; Da, P.; Li, C.; Wang, Z.; Yuan, Z.; Fu, F.; Kawecki, M.; Liu, X.; Sakai, N.; Wang, J. T-W.; Huettner, S.; Buecheler, S.; Fahlman, M.; Gao, F.; Snaith, H. J. Planar perovskite solar cells with long-term stability using ionic liquid additives. *Nature* **2019**, *571*, 245−250.
(12) Xi, J.; Piao, C.; Byeon, J.; Yoon, J.; Wu, Z.; Choi, M. Rational core-shell design of open air low temperature in situ processable $CsPbI_3$ quasi-nanocrystals for stabilized p-i-n solar cells. *Adv. Energy Mater.* **2019**, *9*, 1901787.
(13) Christians, J. A.; Schulz, P.; Tinkham, J. S.; Schloemer, T. H.; Harvey, S. P.; Tremolet de Villers, B. J.; Sellinger, A.; Berry, J. J.; Luther, J. M. Tailored interfaces of unencapsulated perovskite solar cells for > 1,000 h operational stability. *Nat. Energy* **2018**, *3*, 68−74.
(14) Cheacharoen, R.; Rolston, N.; Harwood, D.; Bush, K. A.; Dauskardt, R. H.; McGehee, M. D. Design and understanding of encapsulated perovskite solar cells to withstand temperature cycling. *Energy Environ. Sci.* **2018**, *11*, 144−150.
(15) Said, A. A.; Xie, J.; Zhang, Q. Recent progress in organic electron transport materials in inverted perovskite solar cells. *Small* **2019**, *15*, 1900854.
(16) Wang, N.; Liu, W.; Zhang, Q. Perovskite-based nanocrystals: synthesis and applications beyond solar cells. *Small Methods* **2018**, *2*, 1700380.
(17) Stoumpos, C. C.; Kanatzidis, M. G. Halide perovskites: poor man's high-performance semiconductors. *Adv. Mater.* **2016**, *28*, 5778−5793.
(18) Cao, D. H.; Stoumpos, C. C.; Farha, O. K.; Hupp, J. T.; Kanatzidis, M. G. 2D homologous perovskites as light-absorbing materials for solar cell applications. *J. Am. Chem. Soc.* **2015**, *137*, 7843−7850.
(19) Stoumpos, C. C.; Cao, D. H.; Clark, D. J.; Young, J.; Rondinelli, J. M.; Jang, J. I.; Hupp, J. T.; Kanatzidis, M. G. Ruddlesden-Popper hybrid lead iodide perovskite 2d homologous semiconductors. *Chem. Mater.* **2016**, *28*, 2852−2867.
(20) Tsai, H.; Nie, W.; Blancon, J.-C.; Stoumpos, C. C.; Asadpour, R.; Harutyunyan, B.; Neukirch, A. J.; Verduzco, R.; Crochet, J. J.; Tretiak, S.; Pedesseau, L.; Even, J.; Alam, M. A.; Gupta, G.; Lou, J.; Ajayan, P. M.; Bedzyk, M. J.; Kanatzidis, M. G.; Mohite, A. D. High-efficiency two-dimensional Ruddlesden-Popper perovskite solar cells. *Nature* **2016**, *536*, 312−316.
(21) Quan, L. N.; Yuan, M.; Comin, R.; Voznyy, O.; Beauregard, E. M.; Hoogland, S.; Buin, A.; Kirmani, A. R.; Zhao, K.; Amassian, A.; Kim, D. H.; Sargent, E. H. Ligand-stabilized reduced-dimensionality perovskites. *J. Am. Chem. Soc.* **2016**, *138*, 2649−2655.
(22) Leng, K.; Abdelwahab, I.; Verzhbitskiy, I.; Telychko, M.; Chu, L.; Fu, W.; Chi, X.; Guo, N.; Chen, Z.; Chen, Z.; Zhang, C.; Xu, Q.-H.; Lu, J.; Chhowalla, M.; Eda, G.; Loh, K. P. Molecularly thin two-dimensional hybrid perovskites with tunable optoelectronic properties due to reversible surface relaxation. *Nat. Mater.* **2018**, *17*, 908−914.
(23) Chen, Y.; Sun, Y.; Peng, J.; Tang, J.; Zheng, K.; Liang, Z. 2D Ruddlesden-Popper perovskites for optoelectronics. *Adv. Mater.* **2018**, *30*, 1703487.
(24) Mao, L.; Stoumpos, C. C.; Kanatzidis, M. G. Two-dimensional hybrid halide perovskites: principles and promises. *J. Am. Chem. Soc.* **2019**, *141*, 1171−1190.
(25) Spanopoulos, I.; Hadar, I.; Ke, W.; Tu, Q.; Chen, M.; Tsai, H.; He, Y.; Shekhawat, G.; Dravid, V. P.; Wasielewski, M. R.; Mohite, A. D.; Stoumpos, C. C.; Kanatzidis, M. G. Uniaxial expansion of the 2D Ruddlesden-Popper perovskite family for improved environmental stability. *J. Am. Chem. Soc.* **2019**, *141*, 5518−5534.
(26) Pedesseau, L.; Sapori, D.; Traore, B.; Robles, R.; Fang, H.-H.; Loi, M. A.; Tsai, H.; Nie, W.; Blancon, J.-C.; Neukirch, A.; Tretiak, S.; Mohite, A. D.; Katan, C.; Even, J.; Kepenekian, M. Advances and promises of layered halide hybrid perovskite semiconductors. *ACS Nano* **2016**, *10*, 9776−9786.
(27) Straus, D. B.; Kagan, C. R. Electrons, excitons, and phonons in two-dimensional hybrid perovskites: connecting structural, optical, and electronic properties. *J. Phys. Chem. Lett.* **2018**, *9*, 1434−1447.
(28) Katan, C.; Mercier, N.; Even, J. Quantum and dielectric confinement effects in lower-dimensional hybrid perovskite semiconductors. *Chem. Rev.* **2019**, *119*, 3140−3192.
(29) Smith, M. D.; Connor, B. A.; Karunadasa, H. I. Tuning the luminescence of layered halide perovskites. *Chem. Rev.* **2019**, *119*, 3104−3139.
(30) Mao, L.; Wu, Y.; Stoumpos, C. C.; Wasielewski, M. R.; Kanatzidis, M. G. White-light emission and structural distortion in new corrugated two-dimensional lead bromide perovskites. *J. Am. Chem. Soc.* **2017**, *139*, 5210−5215.
(31) Cortecchia, D.; Neutzner, S.; Kandada, A. R. S.; Mosconi, E.; Meggiolaro, D.; De Angelis, F.; Soci, C.; Petrozza, A. Broadband emission in two-dimensional hybrid perovskites: the role of structural deformation. *J. Am. Chem. Soc.* **2017**, *139*, 39−42.
(32) Mao, L.; Wu, Y.; Stoumpos, C. C.; Traore, B.; Katan, C.; Even, J.; Wasielewski, M. R.; Kanatzidis, M. G. Tunable white-light emission in single-cation-templated three-layered 2D perovskites $(CH_3CH_2NH_3)_4Pb_3Br_{10-x}Cl_x$. *J. Am. Chem. Soc.* **2017**, *139*, 11956−11963.
(33) Yuan, M.; Quan, L. N.; Comin, R.; Walters, G.; Sabatini, R.; Voznyy, O.; Hoogland, S.; Zhao, Y.; Beauregard, E. M.; Kanjanaboos, P.; Lu, Z.; Kim, D. H.; Sargent, E. H. Perovskite energy funnels for efficient light-emitting diodes. *Nat. Nanotechnol.* **2016**, *11*, 872−877.
(34) Wang, N.; Cheng, L.; Ge, R.; Zhang, S.; Miao, Y.; Zou, W.; Yi, C.; Sun, Y.; Cao, Y.; Yang, R.; Wei, Y.; Guo, Q.; Ke, Y.; Yu, M.; Jin, Y.; Liu, Y.; Ding, Q.; Di, D.; Yang, L.; Xing, G.; Tian, H.; Jin, C.; Gao, F.; Friend, R. H.; Wang, J.; Huang, W. Perovskite light-emitting diodes based on solution-processed self-organized multiple quantum wells. *Nat. Photonics* **2016**, *10*, 699−704.
(35) Quan, L. N.; Zhao, Y.; de Arquer, F. P. G.; Sabatini, R.; Walters, G.; Voznyy, O.; Comin, R.; Li, Y.; Fan, J. Z.; Tan, H.; Pan, J.; Yuan, M.; Bakr, O. M.; Lu, Z.; Kim, D. H.; Sargent, E. H. Tailoring the energy landscape in quasi-2D halide perovskites enables efficient green-light emission. *Nano Lett.* **2017**, *17*, 3701−3709.
(36) Quintero-Bermudez, R.; Gold-Parker, A.; Proppe, A. H.; Munir, R.; Yang, Z.; Kelley, S. O.; Amassian, A.; Toney, M. F.; Sargent, E. H. Compositional and orientational control in metal halide perovskites of reduced dimensionality. *Nat. Mater.* **2018**, *17*, 900−907.
(37) Zhang, X.; Ren, X.; Liu, B.; Munir, R.; Zhu, X.; Yang, D.; Li, J.; Liu, Y.; Smilgies, D.-M.; Li, R.; Yang, Z.; Niu, T.; Wang, X.; Amassian, A.; Zhao, K.; Liu, S. Stable high efficiency two-dimensional perovskite solar cells via cesium doping. *Energy Environ. Sci.* **2017**, *10*, 2095−2102.
(38) Qing, J.; Liu, X. K.; Li, M.; Liu, F.; Yuan, Z.; Tiukalova, E.; Yan, Z.; Duchamp, M.; Chen, S.; Wang, Y.; Bai, S.; Liu, J.-M.; Snaith, H. J.; Lee, C.-S.; Sum, T. C.; Gao, F. Aligned and graded type-II Ruddlesden-Popper perovskite films for efficient solar cells. *Adv. Energy Mater.* **2018**, *8*, 1800185.
(39) Zuo, C.; Scully, A. D.; Vak, D.; Tan, W.; Jiao, X.; McNeill, C. R.; Angmo, D.; Ding, D.; Gao, M. Self-assembled 2D perovskite layers for efficient printable solar cells. *Adv. Energy Mater.* **2019**, *9*, 1803258.
(40) Passarelli, J. V.; Fairfield, D. J.; Sather, N. A.; Hendricks, M. P.; Sai, H.; Stern, C. L.; Stupp, S. I. Enhanced out-of-plane conductivity and photovoltaic performance in n = 1 layered perovskites through organic cation design. *J. Am. Chem. Soc.* **2018**, *140*, 7313−7323.
(41) Hoffman, J. M.; Che, X.; Sidhik, S.; Li, X.; Hadar, I.; Blancon, J.-C.; Yamaguchi, H.; Kepenekian, M.; Katan, C.; Even, J.; Stoumpos, C. C.; Mohite, A. D.; Kanatzidis, M. G. From 2D to 1D electronic dimensionality in halide perovskites with stepped and flat layers using propylammonium as a spacer. *J. Am. Chem. Soc.* **2019**, *141*, 10661−10676.
(42) Motti, S. G.; Crothers, T.; Yang, R.; Cao, Y.; Li, R.; Johnston, M. B.; Wang, J.; Herz, L. M. Heterogeneous photon recycling and

charge diffusion enhance charge transport in quasi-2D lead-halide perovskite films. *Nano Lett.* **2019**, *19*, 3953−3960.
(43) Zhang, F.; Kim, D. H.; Lu, H.; Park, J.-S.; Larson, B. W.; Hu, J.; Gao, L.; Xiao, C.; Reid, O. G.; Chen, X.; Zhao, Q.; Ndione, P. F.; Berry, J. J.; You, W.; Walsh, A.; Beard, M. C.; Zhu, K. Enhanced charge transport in 2D perovskites via fluorination of organic cation. *J. Am. Chem. Soc.* **2019**, *141*, 5972−5979.
(44) Lai, H.; Kan, B.; Liu, T.; Zheng, N.; Xie, Z.; Zhou, T.; Wan, X.; Zhang, X.; Liu, Y.; Chen, Y. Two-dimensional Ruddlesden-Popper perovskite with nanorod-like morphology for solar cells with efficiency exceeding 15%. *J. Am. Chem. Soc.* **2018**, *140*, 11639−11646.
(45) Hu, J.; Oswald, I. W. H.; Hu, H.; Stuard, S. J.; Nahid, M. M.; Yan, L.; Chen, Z.; Ade, H.; Neilson, J. R.; You, W. Aryl-perfluoroaryl interaction in two-dimensional organic-inorganic hybrid perovskites boosts stability and photovoltaic efficiency. *ACS Materials Lett.* **2019**, *1*, 171−176.
(46) Li, Z.; Liu, N.; Meng, K.; Liu, Z.; Hu, Y.; Xu, Q.; Wang, X.; Li, S.; Cheng, L.; Chen, G. A new organic interlayer spacer for stable and efficient 2D Ruddlesden-Popper perovskite solar cells. *Nano Lett.* **2019**, *19*, 5237−5245.
(47) Soe, C. M. M.; Nagabhushana, G. P.; Shivaramaiah, R.; Tsai, H.; Nie, W.; Blancon, J.-C.; Melkonyan, F.; Cao, D. H.; Traoré, B.; Pedesseau, L.; Kepenekian, M.; Katan, C.; Even, J.; Marks, T. J.; Navrotsky, A.; Mohite, A. D.; Stoumpos, C. C.; Kanatzidis, M. G. Structural and thermodynamic limits of layer thickness in 2D halide perovskites. *Proc. Natl. Acad. Sci. U. S. A.* **2019**, *116*, 58−66.
(48) Ran, C.; Gao, W.; Li, J.; Xi, J.; Li, L.; Dai, J.; Yang, Y.; Gao, X.; Dong, H.; Jiao, B.; Spanopoulos, I.; Malliakas, C.; Hou, X.; Kanatzidis, M. G.; Wu, Z. Conjugated organic cations enable efficient self-healing $FASnI_3$ solar cells. *Joule* **2019**, *3*, 3072−3087.
(49) Mao, L.; Ke, W.; Pedesseau, L.; Wu, Y.; Katan, C.; Even, J.; Wasielewski, M. R.; Stoumpos, C. C.; Kanatzidis, M. G. Hybrid Dion-Jacobson 2D lead iodide perovskites. *J. Am. Chem. Soc.* **2018**, *140*, 3775−3783.
(50) Slavney, A. H.; Smaha, R. W.; Smith, I. C.; Jaffe, A.; Umeyama, D.; Karunadasa, H. I. Chemical approaches to addressing the instability and toxicity of lead-halide perovskite absorbers. *Inorg. Chem.* **2017**, *56*, 46−55.
(51) Li, X.; Ke, W.; Traoré, B.; Guo, P.; Hadar, I.; Kepenekian, M.; Even, J.; Katan, C.; Stoumpos, C. C.; Schaller, R. D.; Kanatzidis, M. G. Two-dimensional Dion-Jacobson hybrid lead iodide perovskites with aromatic diammonium cations. *J. Am. Chem. Soc.* **2019**, *141*, 12880−12890.
(52) Ishihara, T. Optical properties of PbI-based perovskite structures. *J. Lumin.* **1994**, *60*−*61*, 269−274.
(53) Hanamura, E.; Nagaosa, N.; Kumagai, M.; Takagahara, T. Quantum wells with enhanced exciton effects and optical non-linearity. *Mater. Sci. Eng., B* **1988**, *1*, 255−258.
(54) Stoumpos, C. C.; Kanatzidis, M. G. The renaissance of halide perovskites and their evolution as emerging semiconductors. *Acc. Chem. Res.* **2015**, *48*, 2791−2802.
(55) Stolterfoht, M.; Wolff, C. M.; Márquez, J. A.; Zhang, S.; Hages, C. J.; Rothhardt, D.; Albrecht, S.; Burn, P. L.; Meredith, P.; Unold, T.; Neher, D. Visualization and suppression of interfacial recombination for high-efficiency large-area pin perovskite solar cells. *Nat. Energy* **2018**, *3*, 847−854.
(56) Milot, R. L.; Sutton, R. J.; Eperon, G. E.; Haghighirad, A. A.; Hardigree, J. M.; Miranda, L.; Snaith, H. J.; Johnston, M. B.; Herz, L. M. Charge-carrier dynamics in 2D hybrid metal-halide perovskites. *Nano Lett.* **2016**, *16*, 7001−7007.
(57) Yang, R.; Li, R.; Cao, Y.; Wei, Y.; Miao, Y.; Tan, W. L.; Jiao, X.; Chen, H.; Zhang, L.; Chen, Q.; Zhang, H.; Zou, W.; Wang, Y.; Yang, M.; Yi, C.; Wang, N.; Gao, F.; McNeill, C. R.; Qin, T.; Wang, J.; Huang, W. Oriented quasi-2D perovskites for high performance optoelectronic devices. *Adv. Mater.* **2018**, *30*, 1804771.
(58) Zhang, X.; Munir, R.; Xu, Z.; Liu, Y.; Tsai, H.; Nie, W.; Li, J.; Niu, T.; Smilgies, D.-M.; Kanatzidis, M. G.; Mohite, A. D.; Zhao, K.; Amassian, A.; Liu, S. Phase transition control for high performance Ruddlesden-Popper perovskite solar cells. *Adv. Mater.* **2018**, *30*, 1707166.
(59) Blancon, J.-C.; Tsai, H.; Nie, W.; Stoumpos, C. C.; Pedesseau, L.; Katan, C.; Kepenekian, M.; Soe, C. M. M.; Appavoo, K.; Sfeir, M. Y.; Tretiak, S.; Ajayan, P. M.; Kanatzidis, M. G.; Even, J.; Crochet, J. J.; Mohite, A. D. Extremely efficient internal exciton dissociation through edge states in layered 2D perovskites. *Science* **2017**, *355*, 1288−1292.
(60) Tsai, H.; Asadpour, R.; Blancon, J.-C.; Stoumpos, C. C.; Even, J.; Ajayan, P. M.; Kanatzidis, M. G.; Alam, M. A.; Mohite, A. D.; Nie, W. Design principles for electronic charge transport in solution-processed vertically stacked 2D perovskite quantum wells. *Nat. Commun.* **2018**, *9*, 2130.

https://dx.doi.org/10.1021/jacs.0c09647
J. Am. Chem. Soc. 2020, 142, 19705−19714